

ARTICLE

Received 6 Dec 2013 | Accepted 17 Apr 2014 | Published 20 May 2014

DOI: 10.1038/ncomms4908

Optical hyperpolarization and NMR detection of ^{129}Xe on a microfluidic chip

Ricardo Jiménez-Martínez^{1,2}, Daniel J. Kennedy^{3,4}, Michael Rosenbluh⁵, Elizabeth A. Donley¹, Svenja Knappe¹, Scott J. Seltzer^{3,4}, Hattie L. Ring^{3,4}, Vikram S. Bajaj^{3,4} & John Kitching¹

Optically hyperpolarized ^{129}Xe gas has become a powerful contrast agent in nuclear magnetic resonance (NMR) spectroscopy and imaging, with applications ranging from studies of the human lung to the targeted detection of biomolecules. Equally attractive is its potential use to enhance the sensitivity of microfluidic NMR experiments, in which small sample volumes yield poor sensitivity. Unfortunately, most ^{129}Xe polarization systems are large and non-portable. Here we present a microfabricated chip that optically polarizes ^{129}Xe gas. We have achieved ^{129}Xe polarizations $>0.5\%$ at flow rates of several microlitres per second, compatible with typical microfluidic applications. We employ *in situ* optical magnetometry to sensitively detect and characterize the ^{129}Xe polarization at magnetic fields of $1\mu\text{T}$. We construct the device using standard microfabrication techniques, which will facilitate its integration with existing microfluidic platforms. This device may enable the implementation of highly sensitive ^{129}Xe NMR in compact, low-cost, portable devices.

¹National Institute of Standards and Technology, 325 Broadway, Boulder, Colorado 80305, USA. ²Department of Physics, University of Colorado at Boulder, Boulder, Colorado 80309, USA. ³Materials Science Division, Lawrence Berkeley National Laboratory, Berkeley, California 94720-7300, USA. ⁴Department of Chemistry, University of California at Berkeley, Berkeley, California 94720, USA. ⁵The Jack and Pearl Resnick Institute for Advanced Technology, Department of Physics, Bar-Ilan University, Ramat-Gan IL-52900, Israel. Correspondence and requests for materials should be addressed to V.S.B. (email: vsbajaj@lbl.gov) or to J.K. (email:john.kitching@nist.gov).

Owing to the ease with which it may be placed in a non-equilibrium spin polarization state, ^{129}Xe gas has found extensive use in recent nuclear magnetic resonance (NMR) spectroscopy and magnetic resonance imaging (MRI) experiments, greatly enhancing the resultant NMR signal¹. Furthermore, ^{129}Xe is extremely sensitive to its physiochemical environment, making it a valuable probe on length scales ranging from nanometres to metres². It has enabled new applications ranging from the targeted detection of biomolecules^{3,4} to perfusion imaging of the human lung⁵. However, the large-scale and non-portable nature of ^{129}Xe hyperpolarization hardware precludes its integration into microfluidic platforms, such as have found utility in the miniaturization of numerous analytical techniques⁶. Most ^{129}Xe optical polarizers have been designed to produce litre-sized volumes of polarized gas^{7,8}. These systems, designed for clinical magnetic resonance imaging or the large-scale imaging of materials, are necessarily bulky, expensive and non-portable.

Here, we present the fabrication and operation of a micro-fabricated source of hyperpolarized ^{129}Xe , suitable for the low-cost, power-efficient production of polarized gases and integration with microfluidic systems^{6,9,10}. Our device uses an effective pumping volume of 25 μl and 8 mW of pumping light to achieve ^{129}Xe polarizations $>0.5\%$ at gas flow rates of $5\mu\text{l s}^{-1}$, in the absence of any superconducting magnet. This represents a signal enhancement of ~ 200 over the room temperature thermal equilibrium polarizations achievable at the highest commercially available magnetic field of 23.5 T. Our device requires only standard microfabrication techniques¹¹, benefiting from some of the known strengths of this technology¹², and employs

concurrent high-sensitivity optical magnetometry¹³ to detect the ^{129}Xe NMR signal. Our results are relevant in light of recent innovations in NMR¹⁴, which include sensitivity enhancement through the use of optically hyperpolarized ^{129}Xe gas² and optical magnetometry¹⁵, and the development of microfluidic NMR methods¹⁶. Our device combines all of these technologies in a single chip and may enable the implementation of fully integrated ^{129}Xe NMR instrumentation in low-cost, portable and sensitive lab-on-a-chip devices.

Results

Microfabricated source of hyperpolarized ^{129}Xe . The chip, fabricated from silicon and glass, consists of four chambers 1 mm thick and several millimetres wide connected by micro-channels, as shown in Fig. 1a. A fraction of the ^{129}Xe atoms in the pump chamber (see Fig. 1a) becomes polarized through spin exchange collisions with optically pumped ^{87}Rb atoms at a pumping rate proportional to the ^{87}Rb polarization, P_{Rb} , and the spin-exchange rate, $R_{\text{se}} = n_{\text{Rb}}\gamma_{\text{se}}$, with n_{Rb} being the alkali atomic number density and γ_{se} the ^{87}Rb - ^{129}Xe spin-exchange rate coefficient¹⁷. Under gas flow, polarized ^{129}Xe atoms exit the pump chamber and move through the connecting channel into the probe chamber. Except where stated otherwise, both larger ^{87}Rb atomic density and stronger laser illumination in the pump chamber ensure that the pumping rate of ^{129}Xe in the pump chamber is much larger than that in the probe chamber.

Optical detection of polarized ^{129}Xe . Using the ensemble of ^{87}Rb atoms in the pump and probe chambers as

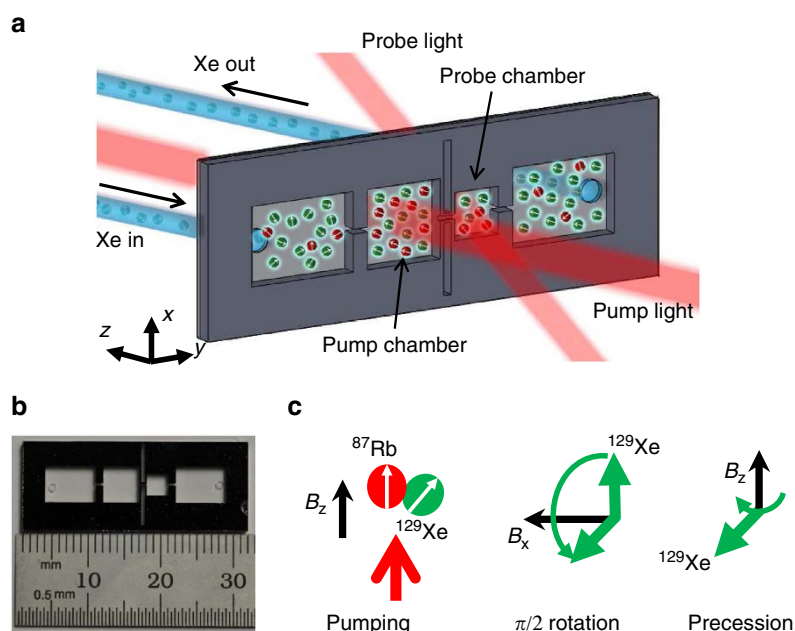


Figure 1 | The microfluidic chip ^{129}Xe polarizer. (a) A gas mixture containing 400 Torr N_2 and 200 Torr Xe in natural isotopic abundance (26.4% ^{129}Xe content) flows from a bulk gas manifold into the inlet chamber, through the pump and probe chambers, and out of the outlet chamber. The chip is loaded with 2 mg of ^{87}Rb metal (see Methods). Unpolarized ^{129}Xe atoms entering the pump chamber become polarized through spin exchange with optically pumped ^{87}Rb . The ^{129}Xe then moves downstream, passes through a microchannel into the probe chamber and eventually exits the device through the output chamber. Optical characterization of the ^{129}Xe polarization in the pump and probe chambers is carried out using the ensemble of ^{87}Rb atoms in each chamber as *in situ* magnetometers. (b) The silicon chip footprint is 3 cm \times 1 cm, with a thickness of 1 mm. The dimensions of the pump and probe chambers are 5 mm \times 5 mm \times 1 mm and 3 mm \times 3 mm \times 1 mm, respectively, whereas the channel connecting the pump and probe chambers is 1 mm \times 0.3 mm \times 0.3 mm. Two tall, narrow grooves are etched from the middle of the chip to provide thermal isolation between the two sides of the device. (c) Pumping and probing sequence for ^{129}Xe . Pumping is carried out continually in the pump chamber in the presence of a longitudinal field of $B_z = 0.8\mu\text{T}$. Every 10–20 s, a transverse DC field of magnitude 5.3 μT is switched on for 4 ms to tip the ^{129}Xe atoms onto the x-y plane and initiate the ^{129}Xe precession about the longitudinal axis.

magnetometers^{13,18,19} sensitive to magnetic fields along the y -axis as defined in Fig. 1a, we detected the ^{129}Xe magnetization, and thus its polarization²⁰, in each chamber as a function of the experimental conditions. The magnitude of the field B_{Rb} sensed by ^{87}Rb due to ^{129}Xe magnetization M_{Xe} is approximately²⁰

$$B_{\text{Rb}} = \frac{2}{3} \mu_0 \kappa_0 M_{\text{Xe}} \quad (1)$$

where μ_0 is the vacuum permeability, $M_{\text{Xe}} = \mu_{\text{Xe}} P_{\text{Xe}} n_{\text{Xe}}$ with μ_{Xe} , P_{Xe} and n_{Xe} being the ^{129}Xe nuclear magnetic moment, polarization and atomic density, respectively. Here, κ_0 represents the enhancement factor due to the Fermi-contact interaction between the valence electron of ^{87}Rb and the ^{129}Xe nuclear spin^{13,18–21}, previously measured to be $\kappa_0 \approx 500$ (ref. 22). Measurement of the ^{129}Xe free-induction decay (FID) in each chamber is made with the magnetometers after rotating the ^{129}Xe longitudinal polarization along the z -axis into the transverse x - y plane with a transverse DC magnetic field pulse, as shown in Fig. 1c.

Figure 2 demonstrates the efficient transport of polarized ^{129}Xe from the pump chamber to the probe chamber while the gas is flowing. Figure 2a shows the measured FID in the pump chamber, obtained by monitoring the transmitted power in the pump beam after the transverse field pulse. Figure 2b shows the measured FID in the probe chamber recorded with the pump beam blocked, so

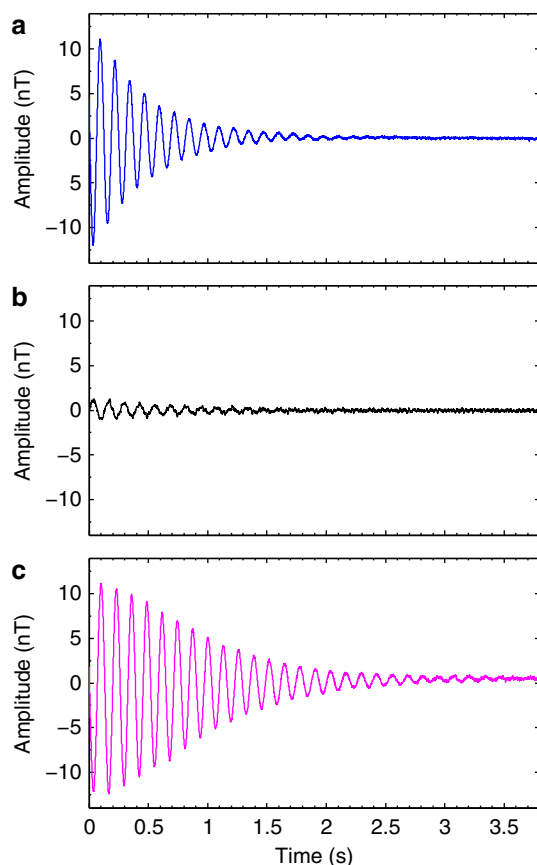


Figure 2 | Transport of polarized ^{129}Xe . (a) Free-induction decay (FID) of the transverse ^{129}Xe polarization in the pump chamber at a total gas flow rate of $3 \mu\text{l s}^{-1}$. (b) FID of polarized ^{129}Xe in the probe chamber with the pump light turned off. (c) FID of polarized ^{129}Xe in the probe chamber with the pump light turned on. Note that for this particular experiment the FID obtained in **b** is 180 degrees out of phase with that obtained in the pump chamber (**a**), due to the use of opposite-handed polarizing photons in the pump and probe chambers.

that there is no flow of polarized ^{129}Xe into the probe chamber. Under these conditions we observe a weak probe FID with amplitude of 1 nT, which we attribute to weak spin-exchange optical pumping (SEOP) of ^{129}Xe by the polarized ^{87}Rb in the probe chamber. Figure 2c shows that the probe FID changes significantly when the pump beam is unblocked; its amplitude increases and its phase changes by 180° to correspond to the amplitude and phase in the pump chamber observed in Fig. 2a. This indicates that the detected ^{129}Xe was polarized in the pump chamber and transported to the probe chamber by the flow of gas.

Characterization of ^{129}Xe polarization. Next, we characterized the ^{129}Xe polarization in the pump and probe chambers as a function of total gas flow rate, alkali atomic density and pumping power. Figure 3a shows the amplitude of the FIDs and the corresponding ^{129}Xe polarization in the pump and probe chambers, which is estimated using $\kappa_0 = 500$ (ref. 22) in equation (1), as a function of total gas flow rate. We observe that the polarization in the pump chamber decreases with flow, while in the probe chamber it builds up, peaks at a flow rate at which the influx of polarized ^{129}Xe is comparable with its spin-relaxation rate, and then follows the pump polarization.

The dependence of the ^{129}Xe polarization in the pump chamber on the alkali atomic density, without gas flow, is shown in Fig. 3b. In our device, relaxation due to ^{129}Xe collisions with the glass walls is much faster than relaxation from spin-exchange collisions. Thus, equation (2.1) (see Methods) predicts a linear relationship between ^{129}Xe polarization and the ^{87}Rb - ^{129}Xe spin-exchange rate, which is proportional to the ^{87}Rb atomic density. This relationship, and a constant ^{87}Rb polarization, can explain the linear behavior of the ^{129}Xe polarization for low alkali atomic densities. At higher alkali densities the ensemble becomes optically thick and, given a finite amount of pumping power, the alkali polarization decreases. As a result the ^{129}Xe polarization no longer increases linearly with alkali density. This limitation can be observed in Fig. 3c, which shows the ^{129}Xe polarization in the pump chamber as a function of pumping power for low and high values of the optical depth OD_0 . At low optical thickness the ^{129}Xe polarization saturates, whereas for the larger optical depth it remains unsaturated at the highest applied optical powers. These results suggest that larger ^{129}Xe polarizations can be achieved by increasing both the ^{87}Rb density and pumping rate.

Discussion

The current polarizations achieved in our device are much lower than the near unity polarizations achieved in some large-scale polarizers^{8,23}. However, as can be extrapolated from Fig. 3b and Fig. 3c, larger polarizations are in principle achievable in our device. We note that the ^{129}Xe relaxation of 1.6 s (see Supplementary Fig. 1 and Supplementary Note 1) observed in our system is 3 to 10 times faster than previously measured in sealed microfabricated cells with 1 mm^3 volume^{24,25}. In this previous work, ^{129}Xe polarizations on the order of 5% were achieved using similar ^{87}Rb densities and slightly larger light intensities than those used in our device. These observations suggest room for improvement in future designs and motivate further study of the limitations of SEOP in microfabricated confinement volumes (see Supplementary Note 2). The combination of higher ^{87}Rb density, greater optical pumping power and improved relaxation times may allow for ^{129}Xe polarizations $>5\%$. The current experiment is designed to produce a large magnetization signal at the expense of polarization through the use of a high ^{129}Xe partial pressure; the use of lower partial pressures is expected to trade off magnetization signal for increased polarization. An important

figure of merit of a polarizer's performance is its spin-transfer efficiency¹; for our device, the spin-transfer efficiency is ~ 0.0038 , competitive with previous polarizers²³, and only one order of magnitude smaller than the largest possible efficiency (see Supplementary Note 3). Another figure of merit is the ratio of the polarized atom flow rate to the optical pumping power. We obtain $0.45 \mu\text{l s}^{-1} \text{W}^{-1}$ for our device, again comparable to this quantity in large-scale polarizers²³ (see Supplementary Table 1).

In this work, we employ the ^{87}Rb atoms as *in situ* detectors^{13,18,19} of the ^{129}Xe magnetization and take advantage of the Fermi-contact interaction^{13,18–21} to enhance the detection sensitivity to ^{129}Xe by a factor of ~ 500 . This approach represents an important feature of our device that can be used to detect or monitor the ^{129}Xe polarization with high sensitivity at low magnetic fields in cases where the polarized gas can be cleanly

extracted from the sample region. If the polarized gas cannot be extracted, as may occur if the gas has been dissolved in a liquid, for example, our device can be easily integrated with microfabricated magnetometers²⁶ placed outside of the pump and probe chambers. Microfabricated magnetometers have demonstrated sensitivities of $5 \text{ fT}/\sqrt{\text{Hz}}$ over bandwidths of 100 Hz ²⁶, enough to detect the magnetic fields due to the currently produced ^{129}Xe polarization, and have been used to detect low-field NMR in microfluidics²⁷. This approach may be useful for applications that are not compatible with the presence of alkali atoms in the microfluidic channels.

We note that conventional glassblowing could also be used to make a compact system capable of producing small quantities of hyperpolarized gas. Compared with the microfabricated silicon-based system we describe here, we expect such a system to be somewhat larger and to require a higher pumping power, but likely to produce larger quantities of more highly polarized gas, due to the weaker wall relaxation and larger pumping volume. While the microfabricated chip described here is not particularly complicated to fabricate, requiring only simple lithography, etching and bonding, a compact glass-blown system may be simpler to implement in a laboratory setting to carry out scientific experiments on microfluidic systems. However, the microfabricated platform will likely be easier to integrate with other silicon-based microfluidic systems due to the common platform material. Microfabrication is likely to be most advantageous in an industrial setting where large numbers of devices might be manufactured. The possibility for large-scale parallel fabrication of devices would likely lead to lower production costs and higher reliability compared with conventional glass-blown systems.

Our device, the first to hyperpolarize ^{129}Xe atoms in one chamber of a microfabricated device and optically interrogate them in another, will enable several new NMR applications without the need for immobile and expensive laboratory-scale instrumentation. We envision the development of portable high-density microfluidic arrays of xenon biosensors for the analysis of complex mixtures^{4,16,28} in confined spaces such as micro-scale chemical reactors, or where access to hyperpolarized ^{129}Xe produced by large-scale polarizers is impractical, such as in field

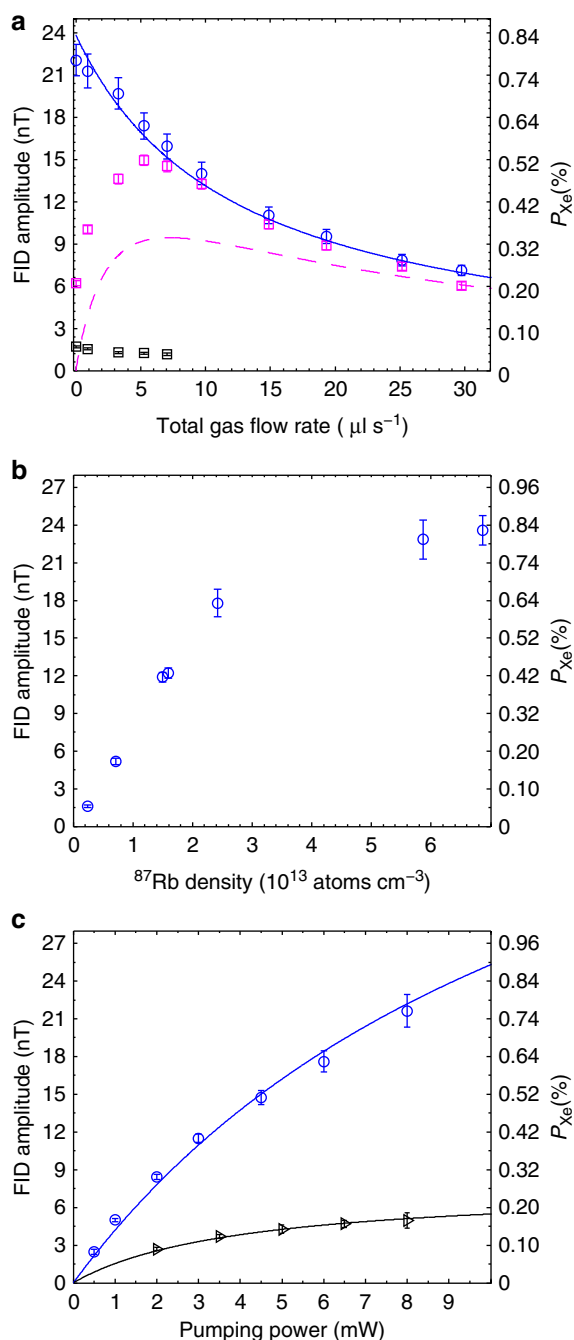


Figure 3 | Device characterization. (a) ^{129}Xe free-induction decay (FID) amplitude as a function of total gas flow rate in the pump chamber (blue circles), in the probe chamber with the pump light on (magenta squares), and with the pump light off (black squares). The solid line corresponds to a fit of the data using equation (2.1) with $R_{\text{se}}^{\text{Pu}}$ as a free parameter and with $R_{\text{Rb}}^{\text{Pu}} = 0.36$ and $R_{\text{wall}}^{\text{Pu}} = (1.6 \text{ s})^{-1}$ (for details see Supplementary Note 1). From the obtained value for $R_{\text{se}}^{\text{Pu}} = 0.012 \text{ s}^{-1}$ and for a ^{87}Rb atomic density of $6 \times 10^{13} \text{ atoms cm}^{-3}$ in the pump chamber, which is estimated from the measured on-resonance optical depth (Methods), we estimate $\gamma_{\text{se}} = 1.7 \times 10^{-16} \text{ cm}^3 \text{ s}^{-1}$, in agreement with reported values for the spin-exchange rate coefficient due to ^{87}Rb - ^{129}Xe binary collisions¹⁷. The dashed line corresponds to the evaluation of equation (2.2) using the fitted value for $R_{\text{Xe}}^{\text{Pu}}$ and $R_{\text{wall}}^{\text{Pr}} = (1.6 \text{ s})^{-1}$; this expression ignores ^{87}Rb - ^{129}Xe spin exchange and neglects the effects of diffusion, which can explain the discrepancy between the estimated line and the data at low flow rates. (b) Pump FID amplitude with no gas flow as a function of ^{87}Rb atomic density and (c) as a function of optical pumping power for $n_{\text{Rb}} = 6 \times 10^{13} \text{ atoms cm}^{-3}$ (blue circles) and $n_{\text{Rb}} = 1 \times 10^{13} \text{ atoms cm}^{-3}$ (black triangles). In c the solid lines correspond to fits to the data using equation (1) and equation (2.1) with $R_{\text{se}}^{\text{Pu}}$ as a fitting parameter and using $R_{\text{wall}}^{\text{Pu}} = (1.6 \text{ s})^{-1}$. The dependence of the Rb polarization was extracted from a fit to the measured shift in the ^{129}Xe Larmor frequency due to the ^{87}Rb magnetization as a function of pumping power (Supplementary Note 1). Error bars are given by 3σ uncertainty in the fit for the FID amplitude.

applications. In such applications, our device would produce hyperpolarized ^{129}Xe for dissolution into a liquid through use of a microfluidic gas-liquid mixer²⁹. The NMR-encoded ^{129}Xe might be removed from the liquid through a microfluidic analogue of a superhydrophobic thin film³⁰ and then detected *in situ* with our integrated magnetometer, enabling extremely high chemical sensitivity, or detected *ex situ* with a physically separate chip-scale atomic magnetometer. Additional experiments suggested for large-scale ^{129}Xe polarizers¹⁴ might also benefit from implementation on our portable, inexpensive device.

Methods

Microfluidic chip fabrication. The device consists of a $3\text{ cm} \times 1\text{ cm} \times 1\text{ mm}$ silicon chip. Deep reactive-ion etching (DRIE) is used to etch four holes of 1 mm depth to form the input, pump, probe and output chambers, as well as the channels connecting the input and output chambers to the pump and probe chambers, respectively. The channel connecting the pump and probe chamber is etched in a subsequent DRIE step. The device is sealed by anodically bonding two slides of borosilicate glass onto the top and bottom surfaces of the silicon chip. The lateral dimensions of the pump and probe chambers are $5\text{ mm} \times 5\text{ mm}$ and $3\text{ mm} \times 3\text{ mm}$, respectively; they are connected by a $1\text{ mm long} \times 300\text{ }\mu\text{m wide} \times 300\text{ }\mu\text{m deep}$ channel. Before being bonded to the chip, one of the glass slides is drilled with holes situated in line with the input and output chambers, through which gas enters and exits the cell. Two $1/8''$ VCR glands are glued onto the glass slide above the holes to allow connection of the cell to a gas manifold. The chip is filled with isotopically enriched ^{87}Rb vapour, produced by the chemical reaction of barium azide and ^{87}Rb chloride³¹ within the input and output chambers as described in Supplementary Note 4.

Experimental setup. The chip is placed inside a two-layer magnetic shield and attached to a gas manifold as shown in Supplementary Fig. 2. Fine control of the gas flow rate through the chip is achieved by a leak valve placed downstream from the chip. Two independently controlled laser beams, tuned to the D1 optical transition of ^{87}Rb at 794.7 nm, irradiate the pump and probe chambers. A distributed feedback laser provides the pump laser beam, whereas light produced by a vertical-cavity surface-emitting laser is used as the probe laser beam. For most of the experiments, the optical power of the pump laser beam was 8 mW, while that in the probe was 100 μW . A set of Helmholtz coils is used to provide transverse magnetic fields in the x and y directions, and a solenoid is used to provide a longitudinal magnetic field in the z -direction. The pump and probe chambers are AC heated using two independent sets of surface mount resistors attached to the cell. The temperature at the input and output chamber is measured using two thermistors that are in close contact with the windows of those chambers. The device operates over a range of temperatures from 120 to 150 °C. The ^{87}Rb atomic density in each chamber is characterized by measuring the optical absorption of the laser beams as their wavelengths are scanned across the D1 optical line of ^{87}Rb . From the measured on-resonance optical depth OD_0 , we calculate the atomic density using $OD_0 = \sigma_0 n_{\text{Rb}} l$ with $l = 1\text{ mm}$ being the length of the beam path inside the pump chamber and $\sigma_0 = 2r_e c f / \Delta\nu$ being the on-resonance optical cross section where $r_e = 2.8 \times 10^{-13}\text{ cm}$ is the classical electron radius, c is the speed of light in vacuum, $f \cong 1/3$ is the oscillator strength of the D1 resonance and $\Delta\nu = 8\text{ GHz}$ is the full-width at half-maximum of the optical line obtained from the fitted optical absorption spectrum.

Model for the ^{129}Xe polarization. The measurements of the ^{129}Xe polarization in the pump $P_{\text{Xe}}^{\text{Pu}}$ and probe $P_{\text{Xe}}^{\text{Pr}}$ chambers can be interpreted in light of a model of the form

$$P_{\text{Xe}}^{\text{Pu}} = \frac{R_{\text{se}}^{\text{Pu}}}{R_{\text{se}}^{\text{Pu}} + R_{\text{wall}}^{\text{Pu}} + R_{\text{flow}}^{\text{Pu}}} P_{\text{Rb}}^{\text{Pu}} \quad (2.1)$$

$$P_{\text{Xe}}^{\text{Pr}} = \frac{R_{\text{flow}}^{\text{Pr}}}{R_{\text{se}}^{\text{Pr}} + R_{\text{wall}}^{\text{Pr}} + R_{\text{flow}}^{\text{Pr}}} P_{\text{Xe}}^{\text{Pu}} \quad (2.2)$$

where the superscripts Pu and Pr indicate the pump and probe chambers, respectively, R_{wall} is the ^{129}Xe spin-destruction rate due to collisions with the chamber walls and R_{flow} is the inverse of the ^{129}Xe transit time through the chamber. These equations are useful for understanding some characteristics of our device and guide future designs. We note, though, that they neglect diffusion, which limits the estimates of equation (2.2) at low flow rates. For example, Fig. 3a demonstrates that, when no gas is flowing, the polarization in the probe chamber is larger when the pump laser is on than when it is off. We have performed experiments, which are described in Supplementary Note 5, indicating that this is due to the transport of polarized ^{129}Xe through diffusion (see Supplementary Figs 3–5). Diffusion is expected to be a uniquely important process for polarization transport in microfluidic systems such as those described here, for which the diffusion length is considerably larger than the characteristic size of the chip.

Atomic magnetometer response and FID estimates. The optically pumped ^{87}Rb magnetometers utilized here are very similar to those discussed in refs 18 and 19. The magnetometers are implemented by introducing a radio-frequency field with 7 kHz modulation frequency and 1 μT amplitude along the y -axis. The signals of the magnetometers are extracted by lock-in detection of the transmitted laser intensity at the modulation frequency. The measured noise floors for the pump and probe magnetometers were $5\text{ pT}/\sqrt{\text{Hz}}$ and $16\text{ pT}/\sqrt{\text{Hz}}$, respectively, with a bandwidth of 40 Hz that is limited by the response of the lock-in amplifiers. This corresponds to a single-shot detection limit of a polarized ensemble of $\sim 5 \times 10^{11}$ ^{129}Xe atoms in each chamber. On resonance, the magnetometers respond linearly to magnetic fields along the y axis that are smaller than the resonance line-width ($\Delta\nu_{\text{HWHM}} \approx 1\text{ }\mu\text{T}$ at zero-light levels dominated by collisions with Xe atoms, and twice or larger with optical pumping). For each change in the device parameters, the linear response of the magnetometers was obtained by extracting the on-resonance slope of the magnetic response acquired by scanning the magnetic field along the y axis. We then used this slope to calibrate the amplitude of the FIDs in magnetic field units. We fit the FID signal in the pump chamber to a single exponentially decaying sinusoid, from which we extracted the amplitude, decay time constant and Larmor precession frequency of ^{129}Xe . We obtained estimates for the FID amplitude in the probe chamber by measuring the amplitude of the first peak and valley in the probe FID signal. Because transverse polarization is transferred from pump to probe chambers as the FID signals are being taken, nonexponential decay of the probe FID can occur, preventing the simple analysis of the data with a single time constant.

References

- Walker, T. G. & Happer, W. Spin-exchange optical pumping of noble-gas nuclei. *Rev. Mod. Phys.* **69**, 629–642 (1997).
- Goodson, B. M. Nuclear magnetic resonance of laser-polarized noble gases in molecules, materials, and organisms. *J. Magn. Reson.* **155**, 157–216 (2002).
- Schröder, L., Lowery, T. J., Hilty, C., Wemmer, D. E. & Pines, A. Molecular imaging using a targeted magnetic resonance hyperpolarized biosensor. *Science* **314**, 446–449 (2006).
- Schröder, L. Xenon for NMR biosensing— inert but alert. *Phys. Med.* **29**, 3–16 (2013).
- Mugler, J. & Altes, T. Hyperpolarized Xe MRI of the human lung. *J. Magn. Reson. Imaging* **37**, 313–331 (2013).
- Whitesides, G. The origins and the future of microfluidics. *Nature* **442**, 368–373 (2006).
- Driehuys, B. *et al.* High volume production of laser polarized ^{129}Xe . *Appl. Phys. Lett.* **69**, 1668–1670 (1996).
- Ruset, I. C., Ketel, S. & Hersman, F. W. Optical pumping system design for large production of hyperpolarized ^{129}Xe . *Phys. Rev. Lett.* **96**, 053002 (2006).
- Dittrich, P. S. & Manz, A. Lab-on-a-chip: microfluidics in drug discovery. *Nat. Rev. Drug Discov.* **5**, 210–218 (2006).
- Yager, P. *et al.* Microfluidic diagnostic technologies for global public health. *Nature* **442**, 412–418 (2006).
- Knappe, S. *et al.* Microfabricated atomic clocks and magnetometers. *J. Opt. A, Pure Appl. Opt.* **8**, S318–S322 (2006).
- Madou, M. J. *Fundamentals of Microfabrication: The Science of Miniaturization* 2nd edn (CRC Press, 2002).
- Savukov, I. M. & Romalis, M. V. NMR detection with an atomic magnetometer. *Phys. Rev. Lett.* **94**, 123001 (2005).
- Harel, E., Schröder, L. & Xu, S. Novel detection schemes of nuclear magnetic resonance and magnetic resonance imaging: applications from analytical chemistry to molecular sensors. *Ann. Rev. Anal. Chem.* **1**, 133–163 (2008).
- Ledbetter, M. P., Savukov, I., Seltzer, S. J. & Budker, D. Detection of nuclear magnetic resonance with atomic magnetometers. in *Optical Magnetometry* (eds Budker, D. & Kimball, J.) Chapter 14 (Cambridge University Press, 2013).
- Bajaj, V. S., Paulsen, J., Harel, E. & Pines, A. Zooming in on microscopic flow by remotely detected MRI. *Science* **330**, 1078–1081 (2010).
- Jau, Y.-Y., Kizma, N. N. & Happer, W. Measurement of ^{129}Xe -Cs binary spin-exchange rate coefficient. *Phys. Rev. A* **69**, 061401 (2004).
- Grover, B. C. Noble-gas NMR detection through noble-gas-rubidium hyperfine contact interaction. *Phys. Rev. Lett.* **40**, 391–392 (1978).
- Volk, C. H., Kwon, T. M. & Mark, J. G. Measurement of the ^{87}Rb - ^{129}Xe spin-exchange cross section. *Phys. Rev. A* **21**, 1549–1555 (1980).
- Schaefer, S. R. *et al.* Frequency shifts of the magnetic-resonance spectrum of mixtures of nuclear spin-polarized noble gases and vapors of spin-polarized alkali-metal atoms. *Phys. Rev. A* **39**, 5613–5623 (1989).
- Herman, R. M. Theory of spin exchange between optically pumped rubidium and foreign gas nuclei. *Phys. Rev.* **137**, A1062–A1065 (1965).
- Ma, Z. L., Sorte, E. G. & Saam, B. Collisional He and Xe frequency shifts in Rb-noble-gas mixtures. *Phys. Rev. Lett.* **106**, 193005 (2011).

23. Nikolau, P. *et al.* Near-unity nuclear polarization with an open-source ^{129}Xe hyperpolarizer for NMR and MRI. *Proc. Natl Acad. Sci. USA* **110**, 14150–14155 (2013).
24. Donley, E. A. *et al.* Nuclear quadrupole resonances in compact vapor cells: the crossover between the NMR and the nuclear quadrupole resonance interaction regimes. *Phys. Rev. A* **79**, 013420 (2009).
25. Donley, E. *et al.* Microfabricated nuclear magnetic resonance gyroscopes: experimental results from three different instruments with varying levels of miniaturization. *Proceedings of the 2009 GOMACTech Conference* (2009).
26. Griffith, W. C., Knappe, S. & Kitching, J. Femtotesla atomic magnetometry in a microfabricated vapor cell. *Opt. Express* **18**, 27167–27172 (2010).
27. Ledbetter, M.P. *et al.* Zero-field remote detection of NMR with a microfabricated atomic magnetometer. *Proc. Natl Acad. Sci. USA* **105**, 2286–2290 (2008).
28. Moule, A. J. *et al.* Amplification of xenon NMR and MRI by remote detection. *Proc. Natl Acad. Sci. USA* **100**, 9122–9127 (2003).
29. de Jong, J., Geerken, M. J., Lammertink, R. G. H. & Wessling, M. Porous microfluidic devices – fabrication and applications. *Chem. Eng. Tech.* **30**, 309–315 (2007).
30. Levkin, P. A., Svec, F. & Fréchet, M. J. Porous polymer coatings: a versatile approach to superhydrophobic surfaces. *Adv. Funct. Mat.* **19**, 1993 (2009).
31. Knappe, S. *et al.* Atomic vapor cells for chip-scale atomic clocks with improved long-term frequency stability. *Opt. Lett.* **30**, 2351–2353 (2005).

Acknowledgements

We thank S. Schima for help with the fabrication of the device, E. Pratt and K. Stupic for useful comments on the manuscript, A. Pines for helpful discussions and L. Jiménez for help in the preparation of Fig. 1. This work is a contribution of the National Institute of Standards and Technology (NIST), an agency of the U.S. government, and is not subject to copyright. Research was supported by the U.S. Department of Energy, Office of Basic Energy Sciences, Division of Materials Science and Engineering under contract No. DE-AC02-05CH11231 (D.J.K., S.J.S., H.L.R. and V.S.B.). R.J.M. was supported in part by the Roberto Rocca Education Program.

Author contributions

All authors contributed extensively to the work presented in this paper.

Additional information

Supplementary Information accompanies this paper at <http://www.nature.com/naturecommunications>

Competing financial interests: The authors declare no competing financial interests.

Reprints and permission information is available online at <http://npg.nature.com/reprintsandpermissions/>

How to cite this article: Jiménez-Martínez, R. *et al.* Optical hyperpolarization and NMR detection of ^{129}Xe on a microfluidic chip. *Nat. Commun.* 5:3908 doi: 10.1038/ncomms4908 (2014).